nanomaterials

MDPI

Article

T_1-Weight Magnetic Resonance Imaging Performances of Iron Oxide Nanoparticles Modified with a Natural Protein Macromolecule and an Artificial Macromolecule

Cheng Tao †, Qiang Zheng †, Lu An, Meie He, Jiaomin Lin *, Qiwei Tian and Shiping Yang *

The Key Laboratory of Resource Chemistry of the Ministry of Education, the Shanghai Key Laboratory of Rare Earth Functional Materials, and the Shanghai Municipal Education Committee Key Laboratory of Molecular Imaging Probes and Sensors, Shanghai Normal University, Shanghai 200234, China; 1000441586@smail.shnu.edu.cn (C.T.); diwuxiaoo@163.com (Q.Z.); anlu1987@shnu.ed.cn (L.A.); 1000441337@smail.shnu.edu.cn (M.H.); qiweitian@shnu.edu.cn (Q.T.)

* Correspondence: linjm@shnu.edu.cn (J.L.); shipingy@shnu.edu.cn (S.Y.); Tel.: +86-64322343 (S.Y.)

† Those authors contributed equally to this work.

Received: 7 January 2019; Accepted: 26 January 2019; Published: 30 January 2019

Abstract: To optimize the iron oxide nanoparticles as T_1-weight contrast for in vivo magnetic resonance imaging (MRI), numbers of macromolecule ligands have been explored with considerable effort. However, reports refer to the comparison of the T_1-weight contrast performances of iron oxide nanoparticles modified with natural and artificial macromolecule ligands are still limited. In this work, we used a typical natural protein macromolecule (bovine serum albumin, BSA) and an artificial macromolecule (poly(acrylic acid)-poly(methacrylic acid), PMAA-PTTM) as surface ligands to fabricate Fe_3O_4-BSA and Fe_3O_4-PMAA-PTTM nanoparticles with similar size and magnetization by the coprecipitation method and compared their MRI performances. In vitro and in vivo experiments revealed that Fe_3O_4-BSA with lower cytotoxicity exhibited higher r_2/r_1 ratio in solution and darkening contrast enhancement for liver and kidney sites of mice under T_1-weight imaging, while Fe_3O_4-PMAA-PTTM displayed much lower r_2/r_1 ratio in solution and brighter contrast enhancement for liver and kidney sites. These remarkably different MRI behaviors demonstrated that the surface ligands play an important role for optimizing the MRI performance of Fe_3O_4 nanoparticles. We expect these results may facilitate the design of macromolecule ligands for developing an iron oxide–based T_1-weight contrast agent.

Keywords: magnetic resonance imaging; T_1-weight contrasts; magnetic nanoparticles; iron oxide; macromolecule ligands

1. Introduction

Magnetic resonance imaging (MRI) has become one of the most powerful imaging techniques because of its capacity to non-invasively render images with high temporal and spatial resolution [1,2]. To obtain high-quality imaging of diseases, contrast agents are often required during MRI scans. Generally, contrast agents are divided into T_1-weighted contrast, which is able to facilitate the spin-lattice relaxation of protons to generate positive (or bright) contrast enhancement, and T_2-weighted contrast, which is able to cause protons in their vicinity to undergo spin–spin relaxation to produce negative (or dark) contrast enhancement [1]. Due to these intrinsic shortcomings (such as false signal from the calcification and metal deposition areas) of T_2-weighted imaging, T_1 contrast agents are general more preferred clinical diagnostic agents [3]. Currently, the T_1 MRI

contrast agents is mainly dominated by the paramagnetic Gd-chelates [4] (including Magnevist (Gd-DTPA), Dotarem (Gd-DTOA), and Eovist (Gd-EOB-DTPA)) and some Mn-based compounds [5,6] and nanoparticles [7]. However, because of the potential risk of these Gd- and Mn- ions in vivo (e.g., nephrogenic systemic fibrosis caused by the release of the Gd ions from the chelate ligands [8]), great efforts have been devoted to develop alternative T_1 contrast agents.

Magnetic iron oxide nanoparticles, which are usually used as T_2 contrast agents [9–14], have recently been proved to be potential T_1 contrast agents when their sizes are down to small diameter (usually <5 nm) [15–22]. These small iron oxide nanoparticles can display excellent T_1 contrast performance owning to their large surface area with five unpaired electrons of iron ions. Besides, because iron ions are naturally found in the human body and serve as an important physiological element for hemoglobin, iron oxide is considered more biocompatible as compared with Gd- and Mn-based compounds and nanoparticles [18,23]. However, the utilization of iron oxide nanoparticles as T_1 contrast agents still remains a significant challenge because they tend to form aggregations under physiological conditions and thus result in intensive T_2 contrast enhancement and the disappearance of T_1 contrast enhancement [24]. To overcome this challenge, great efforts have recently been devoted to explore hydrophilic macromolecule to modify the surface of iron oxide nanoparticles through different approaches [25–27]. Tailoring the surface of nanoparticles with hydrophilic ligands can avoid the aggregation in vivo and also helps to improve their stability, biocompatibility, and in vivo circulation time [28,29]. Therefore, the development of surface ligands is very important for iron oxide-based contrast agent.

With considerable and substantial efforts in the past few years, a number of macromolecule ligands have been explored, and many of them were shown to be promising ligands for optimizing the T_1-weight contrast performance of iron oxide nanoparticles [17,18,26,30–34]. Particularly, bovine serum albumin (BSA) [31,35] and poly(acrylic acid)-poly(methacrylic acid) (PMAA-PTTM) [32,36] represent typical natural protein macromolecules and artificial macromolecules with abundant coordination groups that can interact with metal ions, which have been widely used as surface ligands for modifying nanoparticles for biological application. For example, Li et al. reported a BSA-modified iron oxide nanoparticle with good biocompatibility for in vivo T_1 and T_2-weighted imaging [31]. Lu et al. reported a PMAA-PTTM modified iron oxide nanoparticle showed high water-soluble and good performance of T_1 and T_2-weighted imaging [32]. Nevertheless, reposts refer to the comparison of T_1-weight contrast performances of iron oxide nanoparticles functionalized with these two macromolecules are still limited. In this work, two kinds of iron oxide nanoparticles with similar size and magnetization and surface ligands modified with BSA and PMAA-PTTM, respectively, were fabricated through coprecipitation method, and their cytotoxicity and T_1-weight contrast performances were compared through in vitro and in vivo experiments.

2. Materials and Methods

2.1. Materials

$FeCl_3 \cdot 6H_2O$, $Fe(SO_4)_2 \cdot 7H_2O$, ammonia solution (25%) were obtained from Sigma Aldrich (Shanghai, China). Bovine serum albumin (BSA) was purchased from Amresco (Solon, OH, USA). All reagents were used without further purification. Poly(acrylic acid)-poly(methacrylic acid) (PMAA-PTTM) was prepared according to the reference [36]. Mouse selection and methods of operations were performed in strictly according to the requirements of the Animal Ethics Committee of the Shanghai Normal University and the Institutional Animal Care and Use Committee.

2.2. Synthesis of Fe_3O_4-BSA and Fe_3O_4-PMAA-PTTM Nanoparticles

In a 250 mL three-necked flask, the ligand BSA (138 mg) was added into 50 mL of deionized water and then stirred under nitrogen atmosphere for one hour to remove the oxygen. Then, a solution (2 mL) containing $FeCl_3 \cdot 6H_2O$ (0.082 mmol, 22.3 mg) and $Fe(SO_4)_2 \cdot 7H_2O$ (0.25 mmol, 70 mg) was injected

into the above solution and heated to 90 °C for 5 min, followed by the injection of 5 mL of concentrated ammonia solution under stirred. The mixed solution becomes black immediately, and the reaction was kept at 90 °C for 2 h before cooled down to room temperature. The Fe_3O_4-BSA nanoparticles were obtained through ultrafiltration centrifugation with a 10-k ultra-filtration centrifuge tube for 7–8 times to remove impurities. The finally obtained Fe_3O_4-BSA nanoparticles were dispersed in deionized water and stored at 5 °C for further experiments.

The Fe_3O_4-PMAA-PTTM nanoparticles were prepared similar with that of Fe_3O_4-BSA, except the ligand of BSA was replaced by PMAA-PTTM. The final black solution was also ultrafiltration centrifuged with a 10-k ultra-filtration centrifuge tube for 7–8 times to remove the impurities, and the obtained Fe_3O_4-PMAA-PTTM nanoparticles were also dispersed in deionized water and stored at 5 °C for further experiments.

2.3. Characterization

Powder X-ray diffraction (PXRD) data with scan range of 10–80° were collected on a Bruker X-ray powder diffractometer (D8 ADVANCE, Cu Kα, Brucker, Karlsruhe, Germany). Fourier-transform IR (FT-IR) spectra with recording wavenumber of 400–4000 cm^{-1} and potassium bromide as pressed pellets were recorded on a Nicolet Avatar 370 FT-IR spectrophotometer (Thermo Electron Corporation, Atkinson, NH, USA). Hysteresis loops were obtained from a superconducting quantum interference device (Lake Shore Cryotronics, Inc., Westerville, OH, USA). Transmission electron microscopy images for the nanoparticles were carried out via JEOL JEM-2010 microscopy (JEOL, Tokyo, Japan). The concentrations of iron-ion were determined through high-dispersion inductively coupled plasma atomic emission spectroscopy (ICP, Prodigy, Teledyne Leeman Labs Inc., Hudson, NY, USA). The longitudinal relaxation times (T_1) and transverse relaxation times (T_2) of Fe_3O_4-BSA and Fe_3O_4-PMAA-PTTM were measured with different iron ion concentrations on a 0.5 T magnetic resonance scanner (NMI20, Niumag, Shanghai, China) with parameters of SF, 18 MHz; TW, 8000 ms; SW, 100 kHz; RG, 20 db; DRG1, 3. The longitudinal relaxation rate (r_1) and transverse relaxation rate (r_2) were obtained by a linear fitting of the iron ion concentration and $1/T_1$ and $1/T_2$. T_1-weighted phantom images of Fe_3O_4-BSA and Fe_3O_4-PMAA-PTTM with different concentrations were carried out on the same magnetic resonance scanner. The parameters for T_1-weighted phantom images were following: repetition time (TR), 300 ms and echo time (TE), 0.04 ms.

2.4. In Vitro Cytotoxicity Assay

Mouse breast tumor 4T1 cells were used to assay the cytotoxicity of Fe_3O_4-BSA and Fe_3O_4-PMAA-PTTM nanoparticles. For this study, 4T1 cells were provided from the Shanghai Institutes for Biological Sciences and cultured in Dulbecco's modified eagle medium at 37 °C with 5% CO_2 and 100% humidity for 24 h. The cytotoxicity was evaluated with MTT assays. Typically, 4T1 cells (5×10^4 cells/well) were first plated in 96-well plate for 24 h and then treated with different concentrations of Fe_3O_4-BSA or Fe_3O_4-PMAA-PTTM nanoparticles (0, 12.5, 25, 50, and 100 μg/mL) in DMEM for 12 or 24 h at 37 °C with 5% CO_2. Thiazolyl blue tetrazolium bromide (20 μL, 5 mg/mL) was added to the well and further incubated for four hours. The supernatant of the plate was removed, and the remaining purple formazan crystals were lysed with 150 μL of dimethyl sulfoxide. The absorption of the formazan was determined through a microplate reader (Multiskan MK3, Thermo Fisher Scientific, Waltham, MA, USA) with a microplate reader (Thermo Fisher Scientific, Waltham, MA, USA) as background.

2.5. In Vivo Magnetic Resonance Imaging

In vivo T_1-weighted images of mice were performed on a 0.5 T MRI scanner (Siemens Medical systems, Erlangen, Germany). During imaging, the mice with weigh of about 20 g were anesthetized by intravenous injection with 8% chloral hydrate. The mice were first imaged in different transversal slices to show the heart, liver, and kidney sites and acquire the images as control groups. The mice were

then given an intravenous injection of Fe_3O_4-BSA with a dose of 10 mg [Fe]/Kg [mouse]. After that, time-scale images with time points of 0, 40, 90, and 180 min were obtained with the same transversal slices. The T_1-weighted images of mice that received an intravenous injection of Fe_3O_4-PMAA-PTTM were carried out with the same procedures and injected dose, except the imaging time points were 20, 60, 120, 180, and 240 min. The imaging parameters were the following: (1) field of view, 80 × 80 mm, (2) repetition time (TR), 500 ms, (3) matrix size, 256 × 192 mm (4) echo time (TE), 18 ms, and (5) slice thickness, 3 mm.

3. Results and Discussion

3.1. Synthesis and Characterizations

Coprecipitation is a convenient approach for fabrication of Fe_3O_4 nanoparticles because it can be carried out in aqueous solution and did not required further surfactant change of the as-synthesized nanoparticles to improve their water-solubility. The Fe_3O_4-BSA and Fe_3O_4-PMAA-PTTM nanoparticles were prepared through this approach with ferric and ferrous salt in the presence of ammonia solution (Figure 1a). Transmission electron microscopy (TEM) images show that the average diameters of Fe_3O_4-BSA and Fe_3O_4-PMAA-PTTM nanoparticles are 5.26 ± 1.25 and 4.34 ± 1.54 nm respectively, showing very similar size for both samples (Figure 1b,c). The narrow size distribution of both samples indicates that the BSA and PMAA-PTTM macromolecules are good templates and stabilizers for controlling the formation and growth of the Fe_3O_4 nanoparticles. The crystalline structures of the as-synthesized samples were determined by powder X-ray diffraction (PXRD). As shown in Figure 2a, the diffraction peaks of both samples are found to be well matched with that of the theoretical patterns of Fe_3O_4 (JCPDS No.75-1449), and no other peaks were detected, confirming the successful preparation of the pure phase Fe_3O_4. The obvious diffraction peaks of both samples indicate that the Fe_3O_4 nanoparticles prepared through such one-step coprecipitation approach have high crystallinity, which is important for magnetic nanoparticles. The zeta potential of Fe_3O_4-BSA and Fe_3O_4-PMAA-PTTM were determined to be −13.5 and −51.0 mV, respectively, which is consistent with the negative potential of BSA and PMAA-PTTM (Figure 2b).

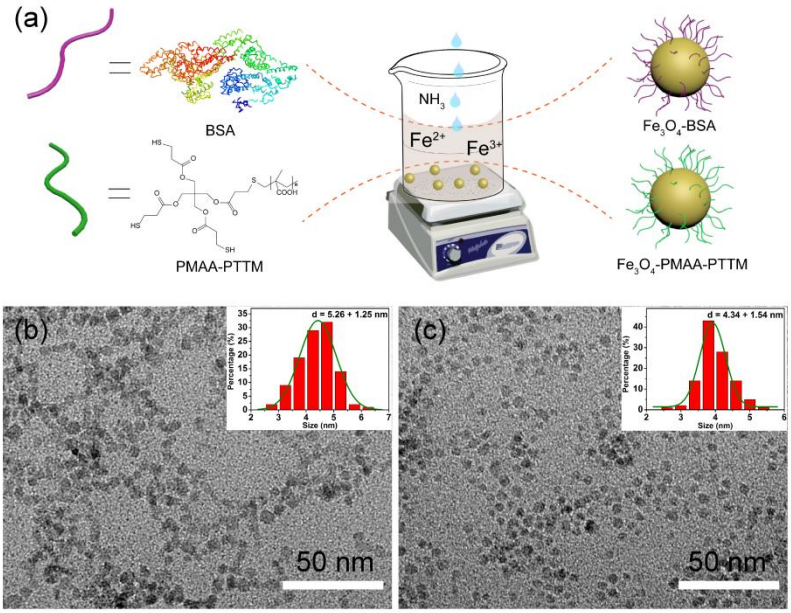

Figure 1. (**a**) Schematic illustration of the fabrication process of Fe_3O_4-BSA and Fe_3O_4-PMAA-PTTM nanoparticles; Transmission electron microscopy (TEM) images of (**b**) Fe_3O_4-BSA and (**c**) Fe_3O_4-PMAA-PTTM nanoparticles.

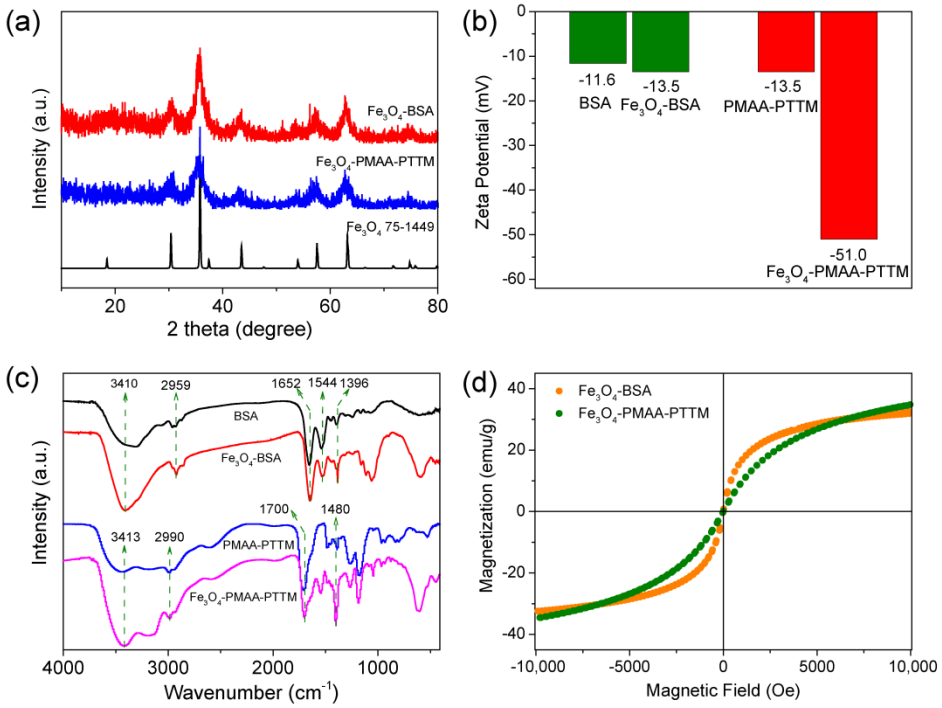

Figure 2. (**a**) Powder X-ray diffraction (PXRD) of Fe_3O_4-BSA (red line), Fe_3O_4-PMAA-PTTM (blue line) and a Fe_3O_4 powder standard (JCPDS Card No. 75-1449, black line); (**b**) Zeta potential of BSA, Fe_3O_4-BSA, PMAA-PTTM and Fe_3O_4-PMAA-PTTM in H_2O; (**c**) Fourier-transform infrared spectroscopy of bovine serum albumin (BSA, black line), Fe3O4-BSA (red line), PMAA-PTTM (blue line) and Fe3O4-PMAA-PTTM (purple line); (**d**) Field-dependent magnetization curves for Fe_3O_4-BSA (yellow dot) and Fe_3O_4-PMAA-PTTM (green dot) nanoparticles at 298 K.

The surface functionalization of the Fe_3O_4 nanoparticles with BSA and PMAA-PTTM ligands were confirmed by Fourier transform infrared (FT-IR) spectrum. As shown in Figure 2c, the BSA displayed characteristic wide absorption peck around 3000–3600 cm^{-1} (O–H and N–H stretching vibrations), and strong absorption peaks at 2959 cm^{-1} (–CH_2– symmetric vibrations), 1652 cm^{-1} (C=O stretching vibrations, amide I), 1544 cm^{-1} (N–H stretching vibrations, amide II), and 1396 cm^{-1} (side chain COO^-) [29]. All of these absorption pecks can also be observed in the FT-IR spectrum of Fe_3O_4-BSA, indicating that the Fe_3O_4 nanoparticles were surface decorated with BSA. For the PMAA-PTTM, characteristic absorption pecks were observed around 3000–3600 cm^{-1} (O–H stretching vibrations), 2990 cm^{-1} (–CH_2– symmetric vibrations), 1700 cm^{-1} (C=O stretching vibrations, amide I), and 1480 cm^{-1} (C–O stretching vibrations of COO^-) [30]. These absorption pecks can be also observed in that of the Fe_3O_4-PMAA-PTTM, demonstrating the presence of PMAA-PTTM macromolecules in the nanoparticles. Besides, the absorption at the 1480 cm^{-1} for the asymmetric C–O stretching vibrations of carboxyl group was lightly shifted to 1550, indicating that the carboxyl groups were coordinated with the Fe ions [22].

Superparamagetism is an important character for Fe_3O_4 nanoparticles to be used as MRI contrast agents. The magnetization curve of Fe_3O_4-BSA and Fe_3O_4-PMAA-PTTM were measured at room temperature using a superconducting quantum interference device with magnetic field up to 1.0 T. As shown in Figure 2d, the coercivity and remanence in hysteresis loops for both Fe_3O_4-BSA and Fe_3O_4-PMAA-PTTM are negligible, indicating they exhibit paramagnetic behavior at room temperature. The saturated magnetization values were determined to be 31.8 and 34.5 emu/g for Fe_3O_4-BSA and Fe_3O_4-PMAA-PTTM, respectively, giving very similar magnetization values for both materials. The similar intrinsic paramagnetic properties of Fe_3O_4-BSA and Fe_3O_4-PMAA-PTTM may enable more convenience for the comparison of their MRI performance.

3.2. In Vitro Magnetic Resonance Imaging

To evaluate the MRI performance, the contrast enhancement properties and relaxation times (T) of Fe_3O_4-BSA and Fe_3O_4-PMAA-PTTM in aqueous solution with different concentrations were determined on a 0.5 T MRI scanner. As showed in Figure 3a–b, for the T_1 phantom images, both Fe_3O_4-BSA and Fe_3O_4-PMAA-PTTM displayed brightening contrast enhancement with the increasing concentration of Fe, indicating that they were T_1 contrast agent at these concentrationa. The longitudinal (r_1) and transverse (r_2) molar relaxivities were calculated according to the equation of $r = \Delta(1/T)/\Delta[Fe]$. The r_1 and r_2 relaxivities of Fe_3O_4-BSA and Fe_3O_4-PMAA-PTTM were 39.3 and 179.8 $mM^{-1}{\cdot}s^{-1}$ and 24.2 and 67.2 $mM^{-1}{\cdot}s^{-1}$, respectively, corresponding to r_2/r_1 ratios of 4.58 and 2.78, respectively. The low r_2/r_1 ratios (below 5.0) of Fe_3O_4-BSA and Fe_3O_4-PMAA-PTTM confirmed that they are adequate for T_1-weighted contrast agents. Compared with Fe_3O_4-BSA, Fe_3O_4-PMAA-PTTM possessed a lower r_2/r_1 ratio, indicating that it is a better T_1 contrast agent [16]. Considering that both Fe_3O_4-BSA and Fe_3O_4-PMAA-PTTM possessed similar particle-sizes and saturated magnetization values, the different relaxivities should be mainly attributed to the effects of the surface decorated ligands. In this context, BSA is a natural protein macromolecule, which not only possessed hydrophilic groups such as carboxyl groups that can coordinated with Fe ions, but also contained abundant hydrophobic side groups that may restrict the diffusion and exchange of water protons (with the coordinated water molecules) surrounding the nanoparticles, and even induce the aggregation of the nanoparticles in the solution, consequently leading to large r_2 relaxivity and r_2/r_1 ratio. In contrast, PMAA-PTTM is a hydrophilic macromolecule, which may be benefit for the surface diffusion and exchange of water protons, and also effectively prevent the aggregation of the nanoparticles, thus result in lower r_2 relaxivity and r_2/r_1 ratio.

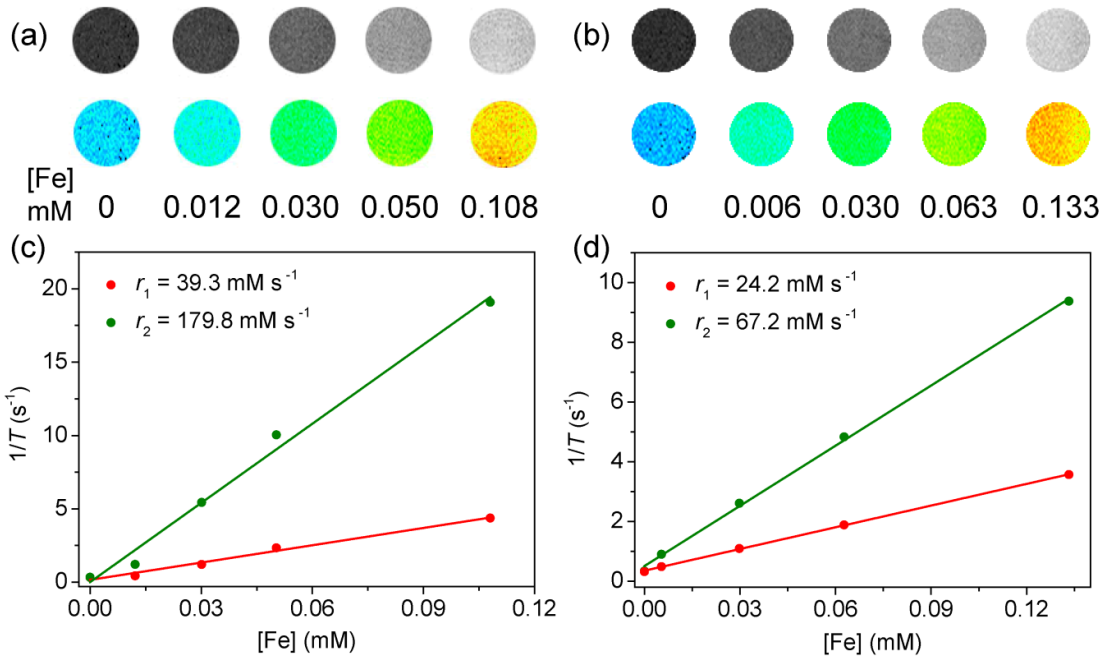

Figure 3. T_1-weight phantom images of (**a**) Fe_3O_4-BSA and (**b**) Fe_3O_4-PMAA-PTTM nanoparticles with various Fe concentrations. Plot of $1/T$ over Fe concentration of (**c**) Fe_3O_4-BSA and (**d**) Fe_3O_4-PMAA-PTTM nanoparticles. The slopes indicate the relaxivity of r_1 (red line) and r_2 (green line).

3.3. In Vitro Cytotoxicity

Before in vivo tests, the cytotoxicity of Fe_3O_4-BSA and Fe_3O_4-PMAA-PTTM were assessed by using a standard methyl thiazolyltetrazolium (MTT) assay with 4T1 (a mouse breast cancer cell line) cell lines. The cell viability after incubation with different concentration of nanoparticles (0–100 $\mu g{\cdot}mL^{-1}$

based on Fe) for 12, 24 and 36 h are showed in Figure 4a. For Fe_3O_4-BSA, the cell viability was almost not affected after incubation for 12 h with the Fe concentration up to 100 μg·mL^{-1}. When the incubation time was prolonged to 36 h (with the same concentration of nanoparticles), the cell viability still remained above 95%. The cell that incubated with Fe_3O_4-PMAA-PTTM also has almost not affected after incubation for 12 h, while when the incubation time were extended to 36, the cell viability slightly dropped to 86% when the concentration of Fe was up to 100 μg·mL^{-1}. These results indicate that both Fe_3O_4-BSA and Fe_3O_4-PMAA-PTTM (less than 100 μg·mL^{-1}) have low cytotoxicity, but Fe_3O_4-BSA is more biocompatible as compared with Fe_3O_4-PMAA-PTTM, which is reasonable since BSA is a natural protein macromolecule.

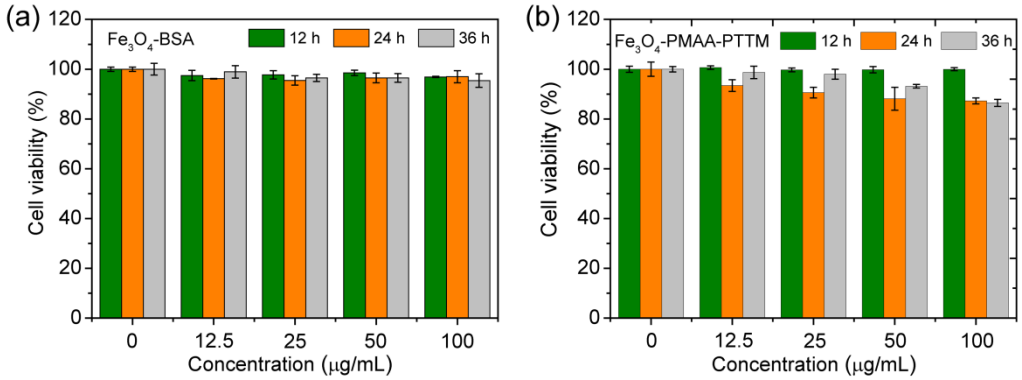

Figure 4. Cell viability of 4T1 cell line after incubation with different concentrations of (**a**) Fe_3O_4-BSA and (**b**) Fe_3O_4-PMAA-PTTM for 12, 24 and 36 h.

3.4. In Vivo Magnetic Resonance Imaging

To compare the MR contrast effect of Fe_3O_4-BSA and Fe_3O_4-PMAA-PTTM, in vivo T_1-weight imaging experiment were performed on a 0.5 T MRI scanner using mice as model. After intravenous injection of Fe_3O_4-BSA/Fe_3O_4-PMAA-PTTM with a dose of 10 mg [Fe]/Kg [mouse], T_1-weight MR images of the coronal planes of mice were acquired at different time points. For Fe_3O_4-BSA, darkening images were observed for the liver and kidney sites after intravenous injection for about 40 min (Figure 5a–b), indicating the Fe_3O_4-BSA displayed T_2 contrast enhancement rather than T_1 contrast enhancement in vivo. To quantify the contrast, the signal-to-noise ratio was calculated by analyzing the liver and kidney sites and the normal tissues of the MR image. As showed in Figure 5c–d, the relative T_1 signals of liver and kidney decreased over time, and reached decreased maximum of at about 180 and 90 min with signals dropped of approximately 55% and 57% for liver and kidney, respectively. The decreased T_1 signals can be can reasonably attributed to the slowly retention and aggregation of Fe_3O_4-BSA nanoparticles in liver and kidney sites, and consequently leading to the change of Fe_3O_4-BSA from T_1 to T_2 contrast agent. After intravenous injection of Fe_3O_4-BSA for about 180 min, the T_1 signals of the kidney sites was slowly recovered to 51%, indicating the slowly metabolism of the Fe_3O_4-BSA from the mice.

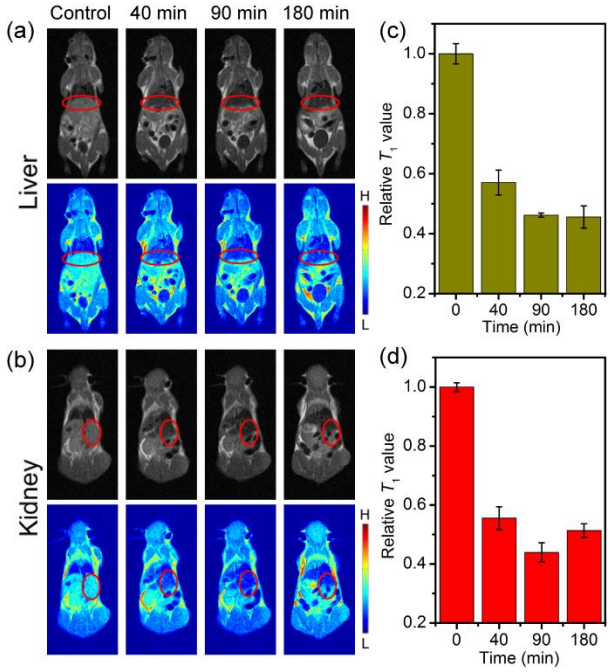

Figure 5. In vivo T_1-weighted magnetic resonance (MR) images of mice (**a**) liver and (**b**) kidney (selected area) collected before (control group) and after intravenous injection of Fe_3O_4-BSA nanoparticles at different time points, and the corresponding relative T_1-weighted signals extracted from (**c**) liver and (**d**) kidney sites.

Different from Fe_3O_4-BSA, brighter images were observed at the liver and kidney sites after intravenous injection for 20 min, indicating that it can enhance T_1 relaxation in vivo (Figure 6a–b). The relative signals extracted from the liver and kidney sites revealed that the signal enhancement in the liver increased over time and reached increased maximum of about 64% at 180 min, while that for the kidney achieved increased maximum of about 47% at 60 min, and then slowly decreased to about 32% at 240 min (Figure 6c–d). The contrast enhancements should be attributed to the slow retention, but not the aggregation, of Fe_3O_4-PMAA-PTTM nanoparticles in the liver and kidney sites. The T_1 signals for liver sites decreased slowly from 240 min, respectively, which indicated the metabolism of the Fe_3O_4-PMAA-PTTM nanoparticles from the mice. These different MRI performances of Fe_3O_4-BSA and Fe_3O_4-PMAA-PTTM suggested that the ligands of the surface of nanoparticles play an important role in the optimizing the T_1 MRI behaviors of nanoparticles in vivo.

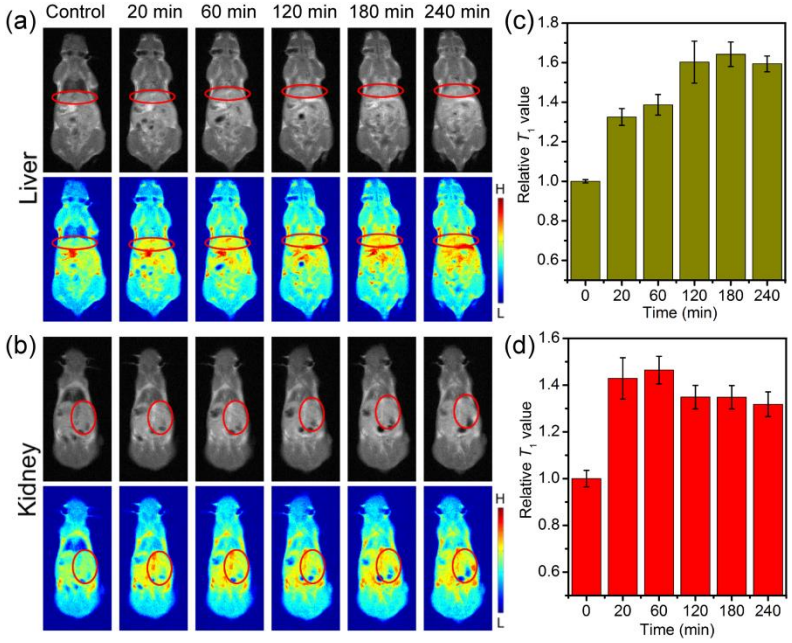

Figure 6. In vivo T_1-weighted MR images of mice (**a**) liver and (**b**) kidney (selected area) collected before (control group) and after intravenous injection of Fe_3O_4-PMAA-PTTM nanoparticles at different time points, and the corresponding relative T_1-weighted signals extracted from (**c**) liver and (**d**) kidney sites.

4. Conclusions

In summary, we have used PMAA-PTTM and BSA as surface ligands to fabricate Fe_3O_4-BSA and Fe_3O_4-PMAA-PTTM nanoparticles with similar size and magnetization by the coprecipitation method and compared their MRI performances in vitro and in vivo. In vitro MRI experiments revealed that Fe_3O_4-PMAA-PTTM has lower r_2/r_1 ratios than that of Fe_3O_4-BSA, but both nanoparticles display T_1-weight contrast enhancement in the solution (under experimental concentration). In vivo T_1-weight imaging revealed that Fe_3O_4-BSA exhibits T_2 contrast enhancement, while Fe_3O_4-PMAA-PTTM exhibits T_1 contrast enhancement at liver and kidney sites, demonstrating that the surface ligands play an important role for the MRI performance of nanoparticles in vivo, which may shed some light on the design of macromolecule ligands for developing an iron oxide–based T_1-weight contrast agent.

Author Contributions: J.L. and S.Y. conceived and designed the experiments; C.T., Q.Z., and M.H. performed the experiments; L.A., Q.T., and J.L. analysed the data; J.L. and S.Y. wrote the pater. All authors discussed the results and commented on the manuscript.

Funding: This research received no external funding.

Acknowledgments: This work was partially supported by the National Natural Science Foundation of China (Nos. 21601124, 21671135 and 21701111), the Shanghai Sailing Program (17YF1413700), the Ministry of Education of China (PCSIRT_IRT_16R49), and the International Joint Laboratory on Resource Chemistry (IJLRC).

Conflicts of Interest: The authors declare no conflict of interest.

References

1. Villaraza, L.A.J.; Bumb, A.; Brechbiel, M.W. Macromolecules, dendrimers, and nanomaterials in magnetic resonance imaging: The interplay between size, function, and pharmacokinetics. *Chem. Rev.* **2010**, *110*, 2921–2959. [CrossRef] [PubMed]
2. Wahsner, J.; Gale, E.M.; Rodríguez-Rodríguez, A.; Caravan, P. Chemistry of MRI contrast agents: Current challenges and new frontiers. *Chem. Rev.* **2019**. [CrossRef] [PubMed]
3. Brown, M.A.; Semelka, R.C. *MRI: Basic Principles and Applications*, 3rd ed.; Wiley: Hoboken, NJ, USA, 2003; pp. 1–280.

4. Caravan, P.; Ellison, J.J.; McMurry, T.J.; Lauffer, R.B. Gadolinium(III) chelates as MRI contrast agents: Structure, dynamics, and applications. *Chem. Rev.* **1999**, *99*, 2293–2352. [CrossRef] [PubMed]
5. Gale, E.M.; Atanasova, I.P.; Blasi, F.; Ay, I.; Caravan, P. A manganese alternative to gadolinium for MRI contrast. *J. Am. Chem. Soc.* **2015**, *137*, 15548–15557. [CrossRef] [PubMed]
6. Yang, Y.; Liu, J.; Liang, C.; Feng, L.; Fu, T.; Dong, Z.; Chao, Y.; Li, Y.; Lu, G.; Chen, M.; et al. Nanoscale metal-organic particles with rapid clearance for magnetic resonance imaging-guided photothermal therapy. *ACS Nano* **2016**, *10*, 2774–2781. [CrossRef]
7. Zhao, Z.; Fan, H.; Zhou, G.; Bai, H.; Liang, H.; Wang, R.; Zhang, X.; Tan, W. Activatable fluorescence/MRI bimodal platform for tumor cell imaging via MnO_2 nanosheet-aptamer nanoprobe. *J. Am. Chem. Soc.* **2014**, *136*, 11220–11223. [CrossRef] [PubMed]
8. Kuo, P.H.; Kanal, E.; Abu-Alfa, A.K.; Cowper, S.E. Gadolinium-based MR contrast agents and nephrogenic systemic fibrosis. *Radiology* **2007**, *242*, 647–649. [CrossRef]
9. Ni, D.; Bu, W.; Ehlerding, E.B.; Cai, W.; Shi, J. Engineering of inorganic nanoparticles as magnetic resonance imaging contrast agents. *Chem. Soc. Rev.* **2017**, *46*, 7438–7468. [CrossRef]
10. Gao, Z.; Hou, Y.; Zeng, J.; Chen, L.; Liu, C.; Yang, W.; Gao, M. Tumor microenvironment-triggered aggregation of antiphagocytosis 99mTc-labeled Fe_3O_4 nanoprobes for enhanced tumor imaging in vivo. *Adv. Mater.* **2017**, *29*, 1701095. [CrossRef]
11. Zhao, Z.; Zhou, Z.; Bao, J.; Wang, Z.; Hu, J.; Chi, X.; Ni, K.; Wang, R.; Chen, X.; Chen, Z.; et al. Octapod iron oxide nanoparticles as high-performance T_2 contrast agents for magnetic resonance imaging. *Nat. Commun.* **2013**, *4*, 2266. [CrossRef]
12. Zhang, Y.; Yang, H.; Zhou, Z.; Huang, K.; Yang, S.; Han, G. Recent advances on magnetic relaxation switching assay-based nanosensors. *Bioconjugate Chem.* **2017**, *28*, 869–879. [CrossRef] [PubMed]
13. Bonvin, D.; Alexander, D.; Millán, A.; Piñol, R.; Sanz, B.; Goya, G.; Martínez, A.; Bastiaansen, J.; Stuber, M.; Schenk, K.; et al. Mionić Ebersold, M. Tuning properties of iron oxide nanoparticles in aqueous synthesis without ligands to improve MRI relaxivity and SAR. *Nanomaterials* **2017**, *7*, 225. [CrossRef] [PubMed]
14. Wang, Y.; Gu, H. Core-shell-type magnetic mesoporous silica nanocomposites for bioimaging and therapeutic agent delivery. *Adv. Mater.* **2015**, *27*, 576–585. [CrossRef] [PubMed]
15. Tromsdorf, U.I.; Bruns, O.T.; Salmen, S.C.; Beisiegel, U.; Weller, H. A highly effective, nontoxic T_1 MR contrast agent based on ultrasmall PEGylated iron oxide nanoparticles. *Nano Lett.* **2009**, *9*, 4434–4440. [CrossRef]
16. Kim, B.H.; Lee, N.; Kim, H.; An, K.; Park, Y.I.; Choi, Y.; Shin, K.; Lee, Y.; Kwon, S.G.; Na, H.B.; et al. Large-scale synthesis of uniform and extremely small-sized iron oxide nanoparticles for high-resolution T_1 magnetic resonance imaging contrast agents. *J. Am. Chem. Soc.* **2011**, *133*, 12624–12631. [CrossRef] [PubMed]
17. Shen, Z.; Wu, A.; Chen, X. Iron oxide nanoparticle based contrast agents for magnetic resonance imaging. *Mol. Pharm.* **2017**, *14*, 1352–1364. [CrossRef] [PubMed]
18. Lee, N.; Yoo, D.; Ling, D.; Cho, M.H.; Hyeon, T.; Cheon, J. Iron oxide based nanoparticles for multimodal imaging and magnetoresponsive therapy. *Chem. Rev.* **2015**, *115*, 10637–10689. [CrossRef] [PubMed]
19. Rui, Y.-P.; Liang, B.; Hu, F.; Xu, J.; Peng, Y.-F.; Yin, P.-H.; Duan, Y.; Zhang, C.; Gu, H. Ultra-large-scale production of ultrasmall superparamagnetic iron oxide nanoparticles for T_1-weighted MRI. *RSC Adv.* **2016**, *6*, 22575–22585. [CrossRef]
20. Luo, Y.; Yang, J.; Yan, Y.; Li, J.; Shen, M.; Zhang, G.; Mignani, S.; Shi, X. RGD-functionalized ultrasmall iron oxide nanoparticles for targeted T1-weighted MR imaging of gliomas. *Nanoscale* **2015**, *7*, 14538–14546. [CrossRef]
21. Liu, C.-L.; Peng, Y.-K.; Chou, S.-W.; Tseng, W.-H.; Tseng, Y.-J.; Chen, H.-C.; Hsiao, J.-K.; Chou, P.-T. One-Step, Room-Temperature Synthesis of Glutathione-Capped Iron-Oxide Nanoparticles and their Application in In Vivo T_1-Weighted Magnetic Resonance Imaging. *Small* **2014**, *10*, 3962–3969. [CrossRef]
22. Huang, J.; Wang, L.; Zhong, X.; Li, Y.; Yang, L.; Mao, H. Facile non-hydrothermal synthesis of oligosaccharide coated sub-5 nm magnetic iron oxide nanoparticles with dual MRI contrast enhancement effects. *J. Mater. Chem. B* **2014**, *2*, 5344–5351. [CrossRef]
23. Liu, G.; Gao, J.; Ai, H.; Chen, X. Applications and potential toxicity of magnetic iron oxide nanoparticles. *Small* **2013**, *9*, 1533–1545. [CrossRef] [PubMed]
24. Wang, L.; Huang, J.; Chen, H.; Wu, H.; Xu, Y.; Li, Y.; Yi, H.; Wang, Y.A.; Yang, L.; Mao, H. Exerting enhanced permeability and retention effect driven delivery by ultrafine iron oxide nanoparticles with T_1–T_2 switchable magnetic resonance imaging contrast. *ACS Nano* **2017**, *11*, 4582–4592. [CrossRef] [PubMed]

25. Xiao, L.; Li, J.; Brougham, D.F.; Fox, E.K.; Feliu, N.; Bushmelev, A.; Schmidt, A.; Mertens, N.; Kiessling, F.; Valldor, M.; et al. Water-soluble superparamagnetic magnetite nanoparticles with biocompatible coating for enhanced magnetic resonance imaging. *ACS Nano* **2011**, *5*, 6315–6324. [CrossRef] [PubMed]
26. Wang, G.; Zhang, X.; Skallberg, A.; Liu, Y.; Hu, Z.; Mei, X.; Uvdal, K. One-step synthesis of water-dispersible ultra-small Fe_3O_4 nanoparticles as contrast agents for T_1 and T_2 magnetic resonance imaging. *Nanoscale* **2014**, *6*, 2953–2963. [CrossRef]
27. Hu, Y.; Mignani, S.; Majoral, J.-P.; Shen, M.; Shi, X. Construction of iron oxide nanoparticle-based hybrid platforms for tumor imaging and therapy. *Chem. Soc. Rev.* **2018**, *47*, 1874–1900. [CrossRef] [PubMed]
28. Song, X.; Gong, H.; Yin, S.; Cheng, L.; Wang, C.; Li, Z.; Li, Y.; Wang, X.; Liu, G.; Liu, Z. Ultra-small iron oxide doped polypyrrole nanoparticles for in vivo multimodal imaging guided photothermal therapy. *Adv. Funct. Mater.* **2014**, *24*, 1194–1201. [CrossRef]
29. Xie, J.; Liu, G.; Eden, H.S.; Ai, H.; Chen, X. Surface-engineered magnetic nanoparticle platforms for cancer imaging and therapy. *Acc. Chem. Res.* **2011**, *44*, 883–892. [CrossRef] [PubMed]
30. Illés, E.; Szekeres, M.; Tóth, I.; Farkas, K.; Földesi, I.; Szabó, Á.; Iván, B.; Tombácz, E. PEGylation of superparamagnetic iron oxide nanoparticles with self-organizing polyacrylate-PEG brushes for contrast enhancement in MRI diagnosis. *Nanomaterials* **2018**, *8*, 776. [CrossRef] [PubMed]
31. Li, D.; Hua, M.; Fang, K.; Liang, R. BSA directed-synthesis of biocompatible Fe_3O_4 nanoparticles for dual-modal T_1 and T_2 MR imaging in vivo. *Anal. Methods* **2017**, *9*, 3099–3104. [CrossRef]
32. Li, Z.; Yi, P.W.; Sun, Q.; Lei, H.; Li Zhao, H.; Zhu, Z.H.; Smith, S.C.; Lan, M.B.; Lu, G.Q. Ultrasmall water-soluble and biocompatible magnetic iron oxide nanoparticles as positive and negative dual contrast agents. *Adv. Funct. Mater.* **2012**, *22*, 2387–2393. [CrossRef]
33. Shen, L.-H.; Bao, J.-F.; Wang, D.; Wang, Y.-X.; Chen, Z.-W.; Ren, L.; Zhou, X.; Ke, X.-B.; Chen, M.; Yang, A.-Q. One-step synthesis of monodisperse, water-soluble ultra-small Fe_3O_4 nanoparticles for potential bio-application. *Nanoscale* **2013**, *5*, 2133–2141. [CrossRef] [PubMed]
34. Borase, T.; Ninjbadgar, T.; Kapetanakis, A.; Roche, S.; O'Connor, R.; Kerskens, C.; Heise, A.; Brougham, D.F. Stable aqueous dispersions of glycopeptide-grafted selectably functionalized magnetic nanoparticles. *Angew. Chem. Int. Ed.* **2013**, *52*, 3164–3167. [CrossRef] [PubMed]
35. An, L.; Yan, C.; Mu, X.; Tao, C.; Tian, Q.; Lin, J.; Yang, S. Paclitaxel-induced ultrasmall gallic acid-Fe@BSA self-assembly with enhanced MRI performance and tumor accumulation for cancer theranostics. *ACS Appl. Mater. Interfaces* **2018**, *10*, 28483–28493. [CrossRef] [PubMed]
36. Li, Z.; Tan, B.; Allix, M.; Cooper, A.I.; Rosseinsky, M.J. Direct coprecipitation route to monodisperse dual-functionalized magnetic iron oxide nanocrystals without size selection. *Small* **2008**, *4*, 231–239. [CrossRef]